The Circulation Associated with a Cold Front. Part I: Dry Case

I. ORLANSKI AND B. B. ROSS

Geophysical Fluid Dynamics Laboratory/NOAA, Princeton University, Princeton, N. J. 08540

(Manuscript received 20 July 1976, in revised form 10 June 1977)

ABSTRACT

The transient behavior of an idealized dry frontal system is investigated using a two-dimensional numerical model. The development of a cross-stream circulation within stationary and moving cold fronts is determined for various frontal and synoptic conditions. In the stationary front, a circulation is generated by symmetric baroclinic instability, but nonlinear effects restrict this circulation to remain very weak. In the moving cold front, the vertical shear of the synoptic wind which advects the front produces an ageostrophic residue as a result of the differential advection of the vertical shear of the frontal jet and the horizontal temperature gradient across the front. This residue, which depends upon the vertical synoptic shear and the thermal wind structure of the frontal system, will generate a cross-stream circulation which maintains the cold front in a quasi-steady state. The resulting motion field is described well by the streamfunction balance equation. The lifting produced by the cross-stream circulation in the moving cold front system may be sufficient to trigger deep convection under favorable conditions in the moisture and synoptic wind fields.

1. Introduction

After the enlightening papers of Bjerknes and his collaborators (1919, 1936) on the theory of polar fronts, many investigations have been published which deal with frontal structure and evolution, including observational, theoretical and numerical studies (e.g., Sanders, 1955; Hoskins and Bretherton, 1972; Williams, 1967). Most theoretical and numerical work has concentrated on problems of frontogenesis. In these cases, solutions are achieved in which initially smooth baroclinic zones are distorted to form a frontal zone through an imposed synoptic deformation field. However, although these frontogenesis investigations are successful in explaining frontal formation, they do not provide a complete picture of the circulation within a fully developed front after frontogenesis has occurred. Williams (1974) considers the generation of such a steady-state circulation by including diffusion effects in a numerical model of a developing front which was produced by a deformation field. An understanding of such cross-stream frontal circulation is important, not only because of its relevance to the basic dynamics of the frontal system, but also because of its role as a triggering mechanism for mesoscale convective phenomena such as prefrontal squall lines.

In the present paper, we will not be concerned with the formation of fronts but rather will assume that a mature frontal system has already formed with the associated jet initially in geostrophic balance with the temperature field. We will then study the influence of cross-stream (directed perpendicular to the jet) horizontal advection upon the dynamics of this front.

Our interests will be somewhat similar to those of Sawyer (1956) and Eliassen (1962) in that we will seek to determine a quasi-steady circulation which develops within the frontal system, but our analysis will differ from theirs in that we will employ an unsteady, nongeostrophic numerical model which does not assume time invariance or quasigeostrophy.

Our treatment of this problem as an initial value problem will allow inertial-gravity waves to be generated as the model responds to the given initial conditions. However, the use of open boundary conditions on the side boundaries of the model will permit propagating waves to escape from the numerical domain. This will then allow the frontal system to evolve to an approximate steady state (reasons for expecting such a steady-state solution will be given in Section 4) with transitory motions superimposed upon it which are maintained by ageostrophic effects within the front. Such oscillations will not necessarily be correlated with the initial conditions.

Unsteady numerical solutions will be presented and discussed for different initial frontal conditions, including the intensity and configuration of the frontal jet wind field, and for different initial profiles of the synoptic wind directed across the front. The evolution of the frontal systems will then be investigated for these different cases in order to relate the characteristic circulation within the front to these synoptic and frontal features.

The numerical model as well as the boundary and initial conditions used will be described in Section 2. The numerical solutions obtained for different synoptic

and frontal conditions are described in Section 3. A review of relevant theories as well as a discussion of our results is presented in Section 4. Finally, conclusions are given in Section 5.

2. Formulation of the numerical model

The mesoscale numerical model to be used here employs either the "deep anelastic" equations as formulated by Ogura and Phillips (1962) or a hydrostatic approximation to these equations. The equations are written in Cartesian coordinates (x,y,z) with the y coordinate running parallel to the axis of the front. The temperature field within the frontal system is determined by a y-velocity jet which is initially in geostrophic balance with the temperature gradient across the front. A synoptic wind $U_g(z)$ advects the front in the x-direction, where U_g is taken to be uniform in x. The potential temperature field is assumed to be of the form $\theta + \theta_g(y,z)$ where $\theta_g = 0$ and $\partial\theta_g/\partial y = (f\theta_0/g)\partial U_g/\partial z$ at $y=0$.

In the present paper, the numerical solution is assumed to be two-dimensional in x and z with all variables uniform in y except for the quantity θ_g, where $\partial\theta_g/\partial y$ is only a function of z ($\partial\theta_g/\partial z$ is neglected compared to $\partial\theta/\partial z$). Hence a streamfunction ψ, along with a vorticity ζ, may be used to represent the velocity field in the $x-z$ plane. Also, the Coriolis parameter f in the mesoscale model is assumed to be constant. Finally, moist processes are neglected here but will be incorporated in this model in the paper of Ross and Orlanski (1977). The resulting equation set is in the form treated by Orlanski et al. (1974) but with radiative heating excluded:

$$\frac{\partial\zeta}{\partial t} - J(\psi,\alpha_0\zeta) = f\frac{\partial v}{\partial z} - \frac{g}{\theta_0}\frac{\partial\theta}{\partial x} + \frac{\partial}{\partial x}\left(K\nu_e\frac{\partial\zeta}{\partial x}\right)$$
$$+ \frac{\partial}{\partial z}\left(\nu_e\frac{\partial\zeta}{\partial z}\right), \quad (2.1)$$

$$\frac{\partial v}{\partial t} - \alpha_0 J(\psi,v) = -f\left(\alpha_0\frac{\partial\psi}{\partial z} - U_g\right)$$
$$+ \frac{\partial}{\partial x}\left(K\nu_e\frac{\partial v}{\partial x}\right) + \frac{\partial}{\partial z}\left(\nu_e\frac{\partial v}{\partial z}\right), \quad (2.2)$$

$$\frac{\partial\theta}{\partial t} - \alpha_0 J(\psi,\theta) + v\frac{\partial\theta_g}{\partial y} = \frac{\partial}{\partial x}\left(K\kappa_e\frac{\partial\theta}{\partial x}\right) + \frac{\partial}{\partial z}\left(\kappa_e\frac{\partial\theta}{\partial z}\right), \quad (2.3)$$

$$\zeta = \alpha_0\frac{\partial^2\psi}{\partial x^2} + \frac{\partial}{\partial z}\left(\alpha_0\frac{\partial\psi}{\partial z}\right), \quad (2.4)$$

where the specific volume

$$\alpha_0 \equiv 1/\rho_0 = \alpha_{\text{surface}}\left(1 - \frac{g}{C_p\theta_0}z\right)^{-[(C_p/C_v)-1]}, \quad (2.5)$$

with the surface specific volume α_{surface} independent of x and ψ defined so that $\partial\psi/\partial z = u/\alpha_0$ and $\partial\psi/\partial x = -w/\alpha_0$. The Jacobian is defined as

$$J(A,B) = (\partial A/\partial x)\partial B/\partial z - (\partial A/\partial z)\partial B/\partial x.$$

Because of the presence of the Laplacian on the right-hand side of the vorticity equation (2.4), an elliptic Poisson's equation must be solved in order to advance the above equation system in time. This is done in the model using a variable coefficient, alternating-direction-implicit (ADI) method (see Young, 1971). However, because horizontal velocities are typically two orders of magnitude larger than vertical velocities in the dry front, numerical comparisons have shown the hydrostatic assumption to be a good approximation in the present case. Therefore in the solutions to be considered here, we have replaced the vorticity expression (2.4) with its hydrostatic equivalent

$$\zeta = \frac{\partial}{\partial z}\left(\alpha_0\frac{\partial\psi}{\partial z}\right). \quad (2.4a)$$

The turbulent fluxes of momentum and heat are parameterized using an eddy viscosity parameterization developed by Orlanski and Ross (1973) and Orlanski et al. (1974) in which the eddy diffusivity takes the form

$$\kappa_e = \begin{cases} \kappa_0\left[1 + C\left(\frac{g|\Delta\theta|(\Delta z)^3}{\theta_0\kappa_0\nu_0}\right)^{\frac{1}{4}}\right], & \Delta\theta < 0 \\ \kappa_0, & \Delta\theta \geqslant 0 \end{cases} \quad (2.6)$$

where $\Delta\theta$ is the local vertical grid-point difference in potential temperature. In the model, $\nu_e = 0.7\kappa_e$, $\nu_0 = 0.7\kappa_0$, and the constant K included in the horizontal flux terms of Eqs. (2.1)–(2.3) has a value of 1000 so that the horizontal eddy viscosity and heat diffusivity are 1000 times larger than their respective vertical values. Typical values of κ_0 and C are 5 m² s⁻¹ and 0.75, respectively.

a. Finite-difference formulation

The finite difference representation of the prognostic equations [(2.1)–(2.4)] is identical to that used by Orlanski et al. (1974). Centered space and time difference approximations are used to represent the space and time derivatives but with diffusion terms lagged one time step. The Jacobians are represented by the difference algorithms of Arakawa (1966) and Lilly (1965) to minimize computational instability. The solution is time-smoothed every 30 time steps to suppress the mode splitting associated with the centered time differencing or leapfrog method used. Finally, the diagnostic equation (2.4a) is solved by the usual method for inverting tridiagonal matrices (see Richtmyer and Morton, 1967).

The model domain is resolved by a grid system which

is uniformly spaced in x but which may be variably spaced in z so as to improve resolution near the surface front. The horizontal increment Δx is 20 km in all cases with 76 points across the span producing a domain width of 1500 km. The vertical stretching is accomplished by transforming the z coordinate in the equations (2.1)–(2.4a) as was done by Orlanski et al. (1974). The mapping which was used in most cases to be presented here (constant grid spacing was also used, primarily for test purposes) involved a log-linear transformation with 51 grid points distributed over 15 km height. (A tropopause was prescribed in the temperature profile at 10 km.) This stretching produced a minimum Δz of 150 m near the surface which increased to 300 m at 5000 m and 400 m at 15000 m, the top of the model.

b. Boundary conditions

The bottom boundary of the model consists of a level, adiabatic surface on which velocity slip is permitted. The adiabatic condition $\partial\theta/\partial z = 0$ is used at the surface $z = 0$ for the potential temperature. In the interior of the model, the velocity component v is primarily in geostrophic balance with the horizontal temperature gradient across the front. Therefore, we have assumed v to be in geostrophic balance at the surface and use the surface boundary condition

$$\partial v/\partial z = (g/f\theta_0)\partial\theta/\partial x \quad \text{at } z = 0. \tag{2.7}$$

The cross-stream circulation, which is represented by streamfunction and vorticity, requires use of the simple boundary condition $\psi = 0$ at the surface. Since the prognostic equation for vorticity involves diffusion terms, a boundary condition for vorticity is also required at the surface. For this condition, we will use either the free-slip condition $\zeta = 0$ or the condition

$$\zeta = \left(\frac{g}{f\theta_0}\right)\left(\frac{\partial\theta/\partial x}{f+\partial v/\partial x}\right)\partial^2\psi/\partial x\partial z \quad \text{at } z = 0, \tag{2.8}$$

which is derived from the balance equation (4.11) without forcing (to be discussed in Section 4) and which assumes that the surface vorticity is compatible with the quasigeostrophic behavior of the interior solution. Solutions obtained using these two different vorticity boundary conditions did not differ significantly.

In the vertical, the numerical domain extends above the tropopause. The intensity of tropospheric dynamics in the model may be sufficient to perturb the lower stratosphere. (This is particularly true in the moist model when deep convection penetrates to the tropopause.) However, the amplitude of these perturbations will be weakened considerably because of the large static stability above the tropopause. Therefore we have chosen to use the rigid lid boundary condition $\psi = $ constant at the top boundary of the model. In addition, the vertical gradients of vorticity ζ, y-velocity v, and

potential temperature θ at the top boundary are always fixed at their initial values.

The side boundary conditions are the most difficult to prescribe since the use of periodic or rigid wall boundary conditions is not appropriate in the present problem. The solutions to be studied are highly time-dependent, and no clear distinction between inflow and outflow boundaries is possible at the left and right boundaries. A complete discussion of open boundary conditions has been given by Orlanski (1976). In his discussion, a numerical phase velocity is computed in the neighborhood of each boundary point and is extrapolated to the boundary. The choice of whether a boundary point exhibits "inflow" or "outflow" behavior is determined by the direction of this phase velocity rather than by the direction of the mean flow. A simplified version of this scheme is used in the present model.

Each variable ϕ at the time step $\tau+1$ and at the boundary point $I = IM$ (where the x index I runs normal to the boundary) is expressed as

$$\phi_{IM}^{\tau+1} = \left[\frac{1-\frac{\Delta t}{\Delta x}C_\phi}{1+\frac{\Delta t}{\Delta x}C_\phi}\right]\phi_{IM}^{\tau-1} + \left[\frac{2\frac{\Delta t}{\Delta x}C_\phi}{1+\frac{\Delta t}{\Delta x}C_\phi}\right]\phi_{IM-1}^\tau, \tag{2.9}$$

where Δt and Δx are the time step and x spatial increment, respectively. The phase velocity C_ϕ is computed as

$$C_\phi = \begin{cases} 0, & C_\phi^* \leqslant 0 \\[2mm] C_\phi^*, & 0 < C_\phi^* < \frac{\Delta x}{\Delta t} \\[2mm] \frac{\Delta x}{\Delta t}, & C_\phi^* \geqslant \frac{\Delta x}{\Delta t}, \end{cases} \tag{2.10}$$

where

$$C_\phi^* = -\frac{\Delta x}{\Delta t}\frac{\phi_{IM-1}^\tau - \phi_{IM-1}^{\tau-2}}{\phi_{IM-1}^\tau + \phi_{IM-1}^{\tau-2} - 2\phi_{IM-2}^{\tau-1}}.$$

The phase velocities for the model variables are computed in the above manner with the exception that the phase velocities for vorticity at both sides and the phase velocity for the temperature at the right side are all fixed at the outflow velocity $\Delta x/\Delta t$. Also when anelastic rather than hydrostatic equations are used, the streamfunction ψ must be computed at the side boundaries and is obtained using the vorticity phase velocity C_ζ.

c. Initial conditions

The evolution of various idealized frontal systems will be discussed in Section 3. The different frontal cases can be divided into two basic configurations which are shown in Figs. 1a and 1b. The first configuration, shown
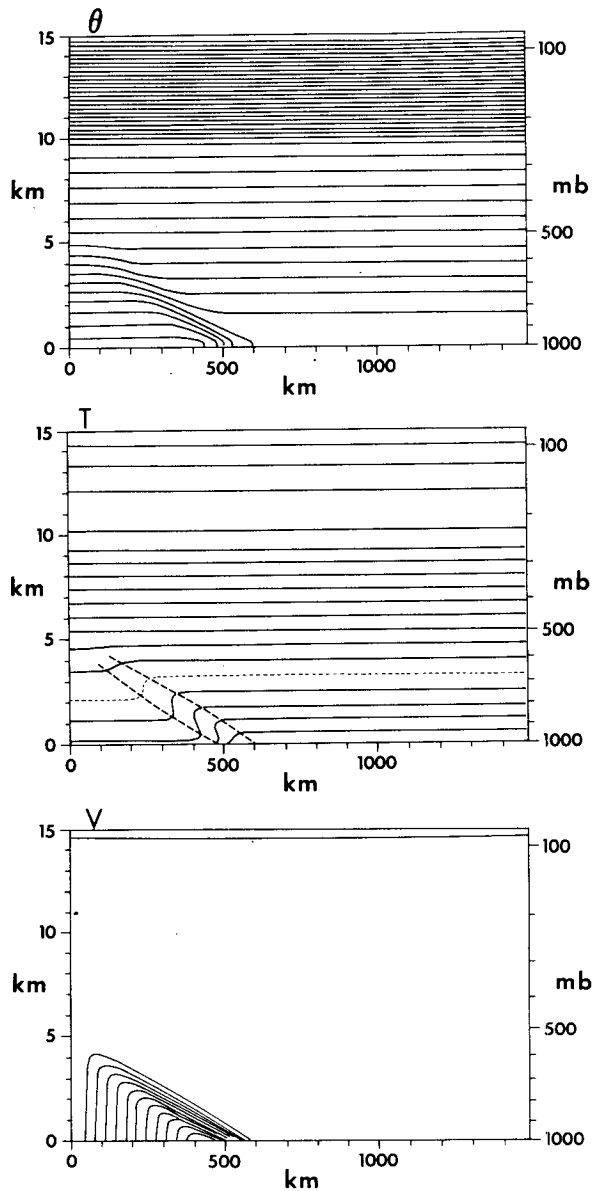
The second configuration is shown in Fig. 1b and will be referred to as the mid-tropospheric jet case (MTJ). The y-velocity v in this case is given as

$$v(x,z) = -(x/x_0)\tfrac{1}{2}V_M\{1-\tanh[\beta(x-\alpha z-x_0)]\}$$
$$+ V_M \exp\{-R_j^{-2}[(z-z_j)^2+(\gamma(x-x_j))^2]\}, \quad (2.12)$$

where x_0, α and β are the same as in (2.11) and $x_j = x_0$, $z_j = 4000$ m, $R_j = (4000/2^{\frac{1}{2}})$ m and $\gamma = 0.03$. The resulting velocity field involves a weak surface jet like the jet used in the first configuration but which has a strong jet centered at 4000 m height and directed in the positive y direction.

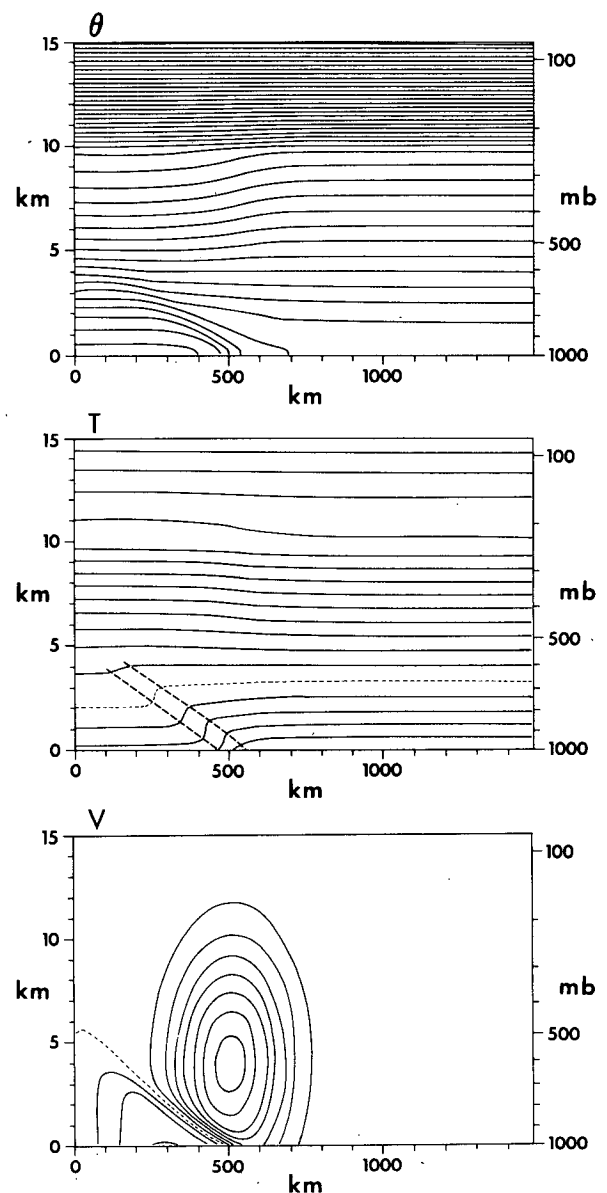The potential temperature field θ is specified so that

FIG. 1a. Initial conditions for surface jet case SJ(45) showing potential temperature θ, temperature T (with boundaries of the frontal region marked), and y-velocity v. Contour intervals are $\Delta\theta = 4°C$, $\Delta T = 5°C$, $\Delta v = 3$ m s^{-1}.

in Fig. 1a, will be referred to as the surface jet case and designated as SJ. In this geometry, the y-velocity field v is given by

$$v(x,z) = -(x/x_0)\tfrac{1}{2}V_M\{1-\tanh[\beta(x-\alpha z-x_0)]\}, \quad (2.11)$$

where x is positive-definite in the model domain, V_M is a jet intensity parameter (to be varied as discussed in the text), $x_0 = 500$ km, $\beta = (50$ km$)^{-1}$ and $\alpha = 100$. As Fig. 1a shows, this produces a jet which has a maximum negative velocity (direction in the negative y direction) at the surface and which is 4000 m deep and approximately 600 km wide.

FIG. 1b. As in Fig. 1a except for mid-tropospheric jet case MTJ(30). Contour intervals are $\Delta\theta = 3°C$, $\Delta T = 5°C$, $\Delta v = 4$ m s^{-1}.

TABLE 1. Initial wind field configurations.

SJ1 (V_M)	$U_g = 0$	$v = -(x/x_0)\frac{1}{2}V_M\{1 - \tanh[f(x,z)]\}$
SJ2 (V_M)	$U_g(z) = 5.00 \, \alpha_0(z) - 2.26$	
SJ3 (V_M)	$U_g(z) = 8.92 \, \alpha_0(z) - 5.61$	[see Eq. (2.11) of text for details]
MTJ1 (V_M)	$U_g = 0$	
MTJ2 (V_M)	$U_g(z) = 2.00 + 3.00 \, \tanh(z/5000)$	$v = -(x/x_0)\frac{1}{2}V_M\{1 - \tanh[f(x,z)]\}$
		$\quad + V_M \exp[g(x,z)]$
MTJ3 (V_M)	$U_g(z) = 8.92 \, \alpha_0(z) - 5.61$	[see Eq. (2.12) of text for details]
MTJ2W (V_M)	$U_g(z) = 2.00 + 3.00 \, \tanh(z/5000)$	$v = (\tilde{x}/x_0)\frac{1}{2}V_M\{1 - \tanh[f(\tilde{x},z)]\}$
		$\quad - V_M \exp[g(\tilde{x},z)],$
		where $\tilde{x} = \text{constant} - x$.

* Specific volume $\alpha_0(z)$ is defined in Eq. (2.5) of the text.

the horizontal gradient $\partial\theta/\partial x$ is in geostrophic balance with the vertical shear of v as specified in each of the two configurations. The vertical variation of θ is prescribed at the rightmost boundary (on the warm side of the front) with lapse rates of $2\times10^{-3}°\text{C m}^{-1}$ for $z < 2000$ m, $4\times10^{-3}°\text{C m}^{-1}$ for 2000 m $< z < 10\,000$ m, and $14.5\times10^{-3}°\text{C m}^{-1}$ for $z > 10\,000$ m. The surface temperature θ_0 at the right boundary then determines $\theta(z)$, and this profile, together with the geostrophic constraint on $\partial\theta/\partial x$ provided by the given field $v(x,z)$ (depending on the parameter V_M), defines the potential temperature fields shown in Figs. 1a and 1b. The resulting frontal systems shown in the two cases give typical horizontal temperature gradients of $12°\text{C}$ over 200 km for the jet intensity values V_M of 45 m s^{-1} for the case SJ and 30 m s^{-1} for the case MTJ.

In addition to the basic geostrophic flow in the y direction, a flow $U_g(z)$ in the x direction is imposed on the initial flow field. This velocity simulates synoptic-scale winds which advect the frontal system. Different intensities and functional forms of this wind field $U_g(z)$ have been used in the solution to be discussed in Section 3.

Table 1 summarizes the different values of the y-jet intensity y_M and the different functional forms of $U_g(z)$ which have been used in the numerical solution for the SJ and MTJ cases to be discussed in Section 3. The different solutions will be identified by the letter-number string shown in the table followed by the value of the jet intensity magnitude V_M enclosed in parentheses [e.g., SJ1 (22.5), MTJ2 (30)]. Included in the table is one warm front case MTJ2W which will be described at the end of Section 3.

3. Description of numerical solutions

The various numerical solutions whose initial and boundary conditions were described in the previous section will be considered with regard to the surface jet and mid-tropospheric jet configurations.

a. Surface jet case (SJ)

The surface jet configuration represents cold and warm air masses which are separated by a frontal

system with a jet whose wind maximum occurs at the surface. Although this frontal jet would be unlikely to occur in the real atmosphere due to surface friction and planetary boundary layer modification, it will be valuable for us to compare the dynamics of this system with the dynamics of more realistic fronts. The use of different magnitudes of cross-stream wind shear and jet amplitude produced markedly different cross-stream circulations.

A typical behavior of the evolution of the cross-stream flow field is shown in Fig. 2 for the strong shear case SJ3(45). [In the nomenclature of Section 2 and Table 1, this is the surface jet case with the frontal jet parameter $V_M = 45$ in Eq. (2.11) and with the initial cross-stream wind $U_g(z) = 8.92\alpha_0 - 5.61$.] The front is shown in this figure to be advected to the right by the mean shear flow with a circulation generated in the $x-z$ plane. This circulation can be seen in the time sequence shown in Fig. 2. The frames to the left show composite contour maps of potential temperature θ and perturbation streamfunction $\psi' = \psi - \psi_g$ at three different times $t = 3.00$, 11.43 and 19.43 h where θ and ψ' are represented by solid and dashed contours, respectively. [The streamfunction ψ_g is defined such that $U_g(z) = \alpha_0 d\psi_g/dz$.] The frames on the right show composite maps, at corresponding times, of the velocity component v along the front (solid lines) and the total streamfunction ψ (dashed lines).

Two major cells are seen to develop in the perturbation streamfunction by the time $t = 3.0$ h soon after the numerical solution begins. (The symbols X and N denote respective locations of maximum and minimum ψ' in the left figures and maximum and minimum v in the right figures.) These cells intensify until a quasi-equilibrium is achieved in which the cells coexist with the moving frontal system. Inertial-gravity wave oscillations can also be detected superimposed upon this system which have horizontal scales on the order of those of the frontal system and a period of approximately 15 h. The vorticity ζ within these cells (as defined in Section 2 as the y vorticity component $(\partial u/\partial z) - (\partial w/\partial x)$ directed along the surface front) is negative on the warm side of the front and positive on
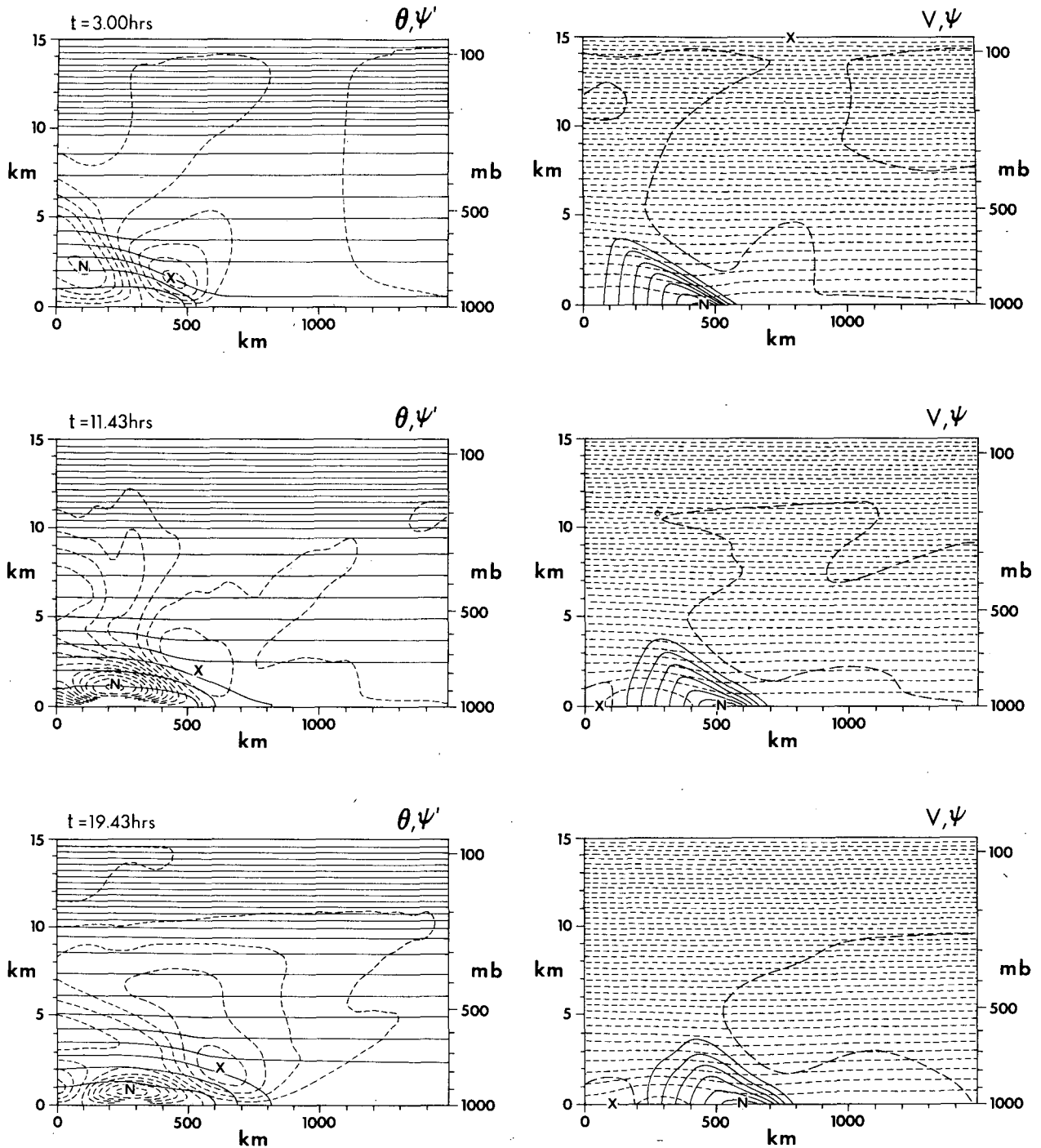
FIG. 2. Time sequence from surface jet case SJ3(45). Left frames show potential temperature θ (solid contours) and perturbation streamfunction ψ' (dashed contours) with X and N denoting locations of maximum and minimum ψ'. Right frames show y-velocity v (solid contours with long dashed contours for zero lines) and total streamfunction ψ (short-dashed contours) with X and N denoting locations of maximum and minimum v. Contour intervals are as follows: $\Delta\theta = 5 \,°C$, $\Delta\psi' = 250 \text{ kg (m s)}^{-1}$, $\Delta v = 5 \text{ m s}^{-1}$, $\Delta\psi = 2000 \text{ kg (m s)}^{-1}$.

the cold side of the front. As shown by the ψ contours in Fig. 2, the effect of this vorticity above the front is to cause air parcels to sink as they pass over the frontal surface. On the other hand, the counterflow near the surface which is caused by the positive vorticity on the cold side of the front reduces the cross-stream advection of cold air parcels close to the ground. This localized blocking effect ultimately produces the domed shape of

the potential temperature contours as seen in Fig. 2 at 19.43 h. The correlation of regions of strong cross-stream vorticity with regions of strong horizontal shear in the jet velocity v is evident in the figure and will be discussed in Section 4.

Unquestionably the strong shear of the cross-stream flow $U_\theta(z)$ plays an important role in determining the ultimate intensity of the cross-stream circulation. Fig. 3 shows a comparison of the perturbation streamfunction contours for three different solutions at the same time and involving the same surface jet con-
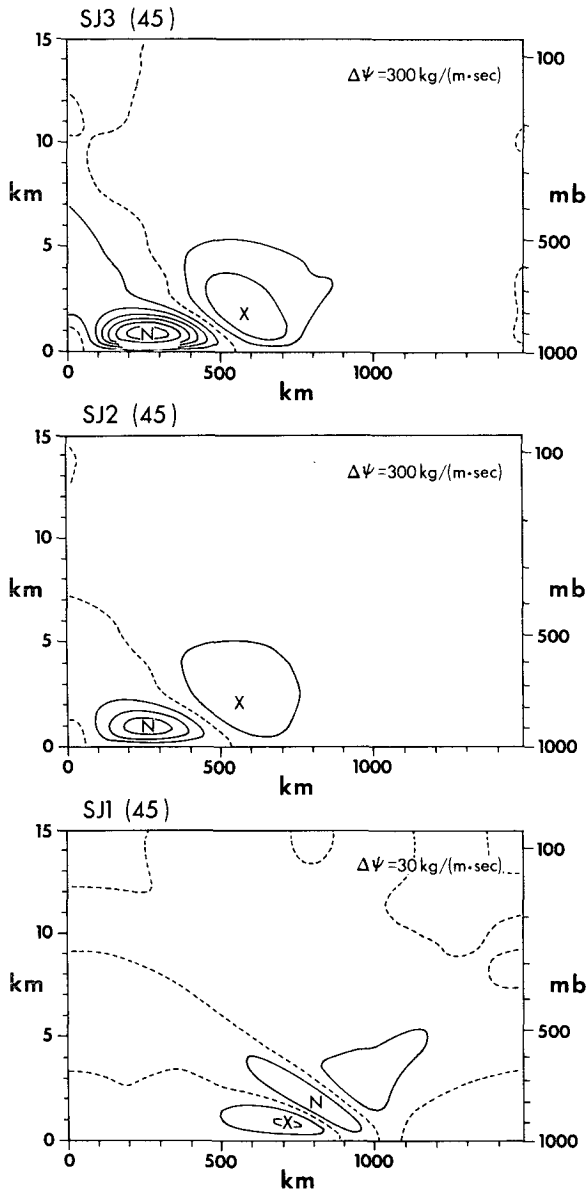

FIG. 3. Comparison of perturbation streamfunction ψ' fields for surface jet cases at time $t=16.80$ h with different shear in the mean cross-stream wind: strong shear SJ3(45), weak shear SJ2(45), and no shear SJ1(45). Contour interval is given in upper right corner of each frame.
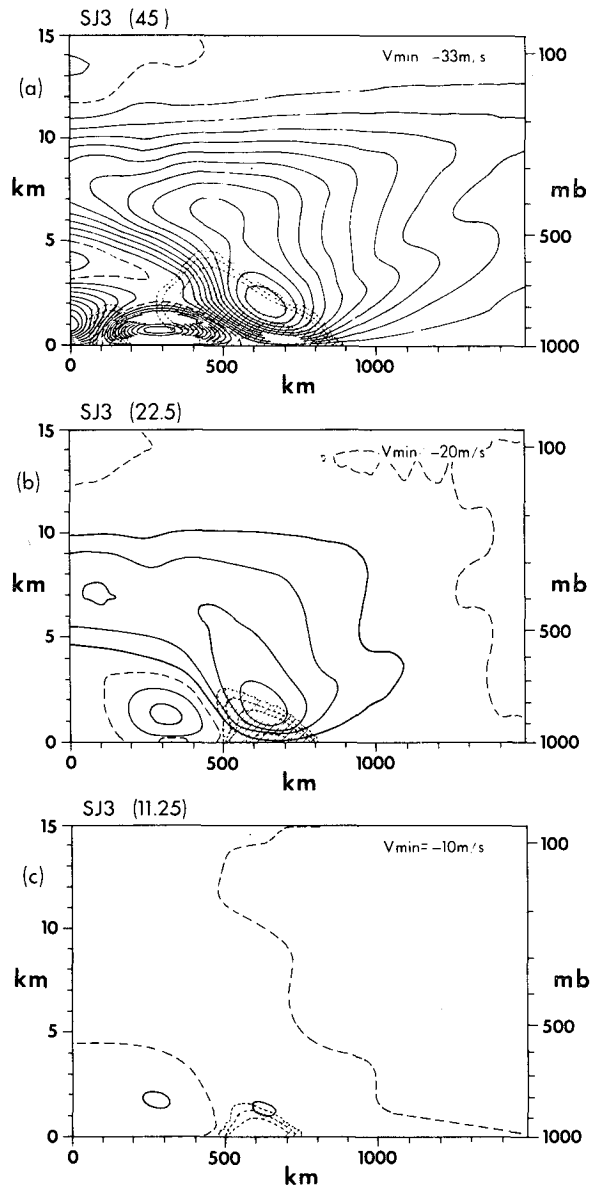

FIG. 4. As in Fig. 3 except at time $t=20.10$ h with different jet intensities V_M (values shown in parentheses in upper left corner of each frame). Cross-hatched areas show regions in which Richardson number $Ri_v < 31$ with the short-dashed contours showing lines of Ri_v in increments of 10. Contour interval $\Delta\psi' = 100$ kg (m s)$^{-1}$.

figuration and its intensity $V_M = 45$ but for three different shears of U_θ: strong shear SJ3(45), weak shear SJ2(45), and no shear SJ1(45). The results for the strong and weak shear cases show the magnitude of the shear to strongly affect the cross-stream circulation intensity. However, the lower frame of Fig. 3 shows that the limiting case of zero shear in U_θ is not, as might be expected, free of cross-stream circulation. On the other hand, the intensity of the circulation which does occur in the absence of shear is far weaker than that
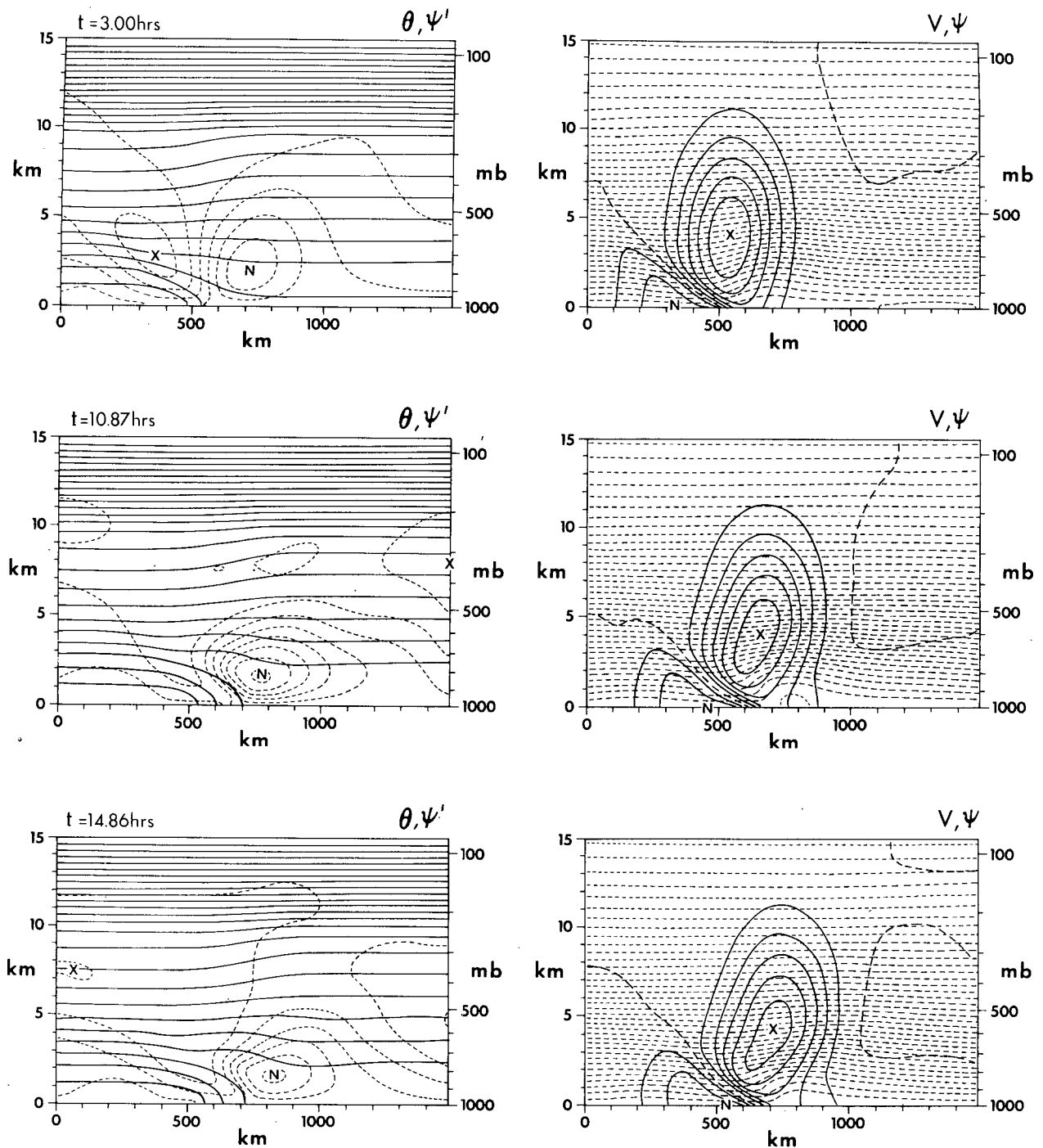
FIG. 5. Time sequence from mid-tropospheric jet case MTJ2(30). Format as in Fig. 2. Contour intervals are as follows: $\Delta\theta = 5$ °C, $\Delta\psi' = 500$ kg (m s)$^{-1}$, $\Delta v = 5$ m s^{-1}, $\Delta\psi = 1000$ kg (m s)$^{-1}$.

which occurs in the presence of shear. The difference in the circulation with and without shear and the fact that a circulation actually does occur in the absence of mean shear are key points in our understanding of frontal circulations and will be considered in detail in the next section.

Another important parameter in the development of the cross-stream circulation is the intensity of the vertical shear of the y velocity component v along the front or, in terms of nondimensional parameters, the magnitude of the local frontal Richardson number Ri_v

defined as

$$\mathrm{Ri_v} = \frac{g}{\theta_0} \frac{\partial\theta/\partial z}{(\partial v/\partial z)^2}.$$

Fig. 4 shows the regions of small Richardson number $\mathrm{Ri_v}$ (as indicated by dashed contours within the areas of crosshatched shading) and contours of perturbation stream function ψ' (solid contours) for three different values of the jet amplitude parameter V_M for the surface jet cases at the time $t = 20.10$ h. All three solutions used the initial strong shear of the cross-stream wind U_g in class SJ3. It is clear from the figure that the intensity of the circulation decreases in proportion to the decrease in the area of low $\mathrm{Ri_v}$. However it is important to note that the directions and the locations of the circulation cells are unaltered as the low-Richardson-number area is reduced.

b. Mid-tropospheric jet case (MTJ)

An analysis of frontal evolution which is similar to that of the surface jet case can be made for the more realistic case of the mid-tropospheric jet configuration. In this case as in the surface jet case, the shear of the mean flow will produce a strong circulation within the frontal system. However, both qualitative and quantitative differences from the former case can be noticed in the development of this circulation. Fig. 5 shows a time sequence of composite contour maps similar in format to Fig. 2 but for the case MTJ2(30) which involves comparable mean frontal wind shear in the jet wind v (which thereby produces a similar horizontal gradient of potential temperature because of the initial geostrophic balance) and in the vertical shear in the initial cross-stream wind U_g at the level of the front. Even though the vertical shears of U_g and v are roughly similar for this case and the case SJ3(45), the cross-stream circulation is far more intense for the mid-tropospheric configuration compared to the surface jet solution. Even more important is the fact that a cell of positive vorticity now lies on the warm air side of the front rather than on the cold side as was the case in the SJ configuration.

As a consequence, this circulation produces a blocking effect near the surface downwind of the surface front, thereby lifting air parcels ahead of the front. This lifting will be of primary importance to the generation of deep convection when the warmer air ahead of the front is moist unstable. [The generation of prefrontal squall lines by this mechanism is treated in detail by Ross and Orlanski (1977).]

The correlation of the vertical shear of the initial cross-stream wind U_g to the intensity of the cross-stream circulation is similar in the mid-tropospheric case to that of the surface jet configuration. Also, a non-zero circulation is observed in the limit of zero cross-stream wind shear.

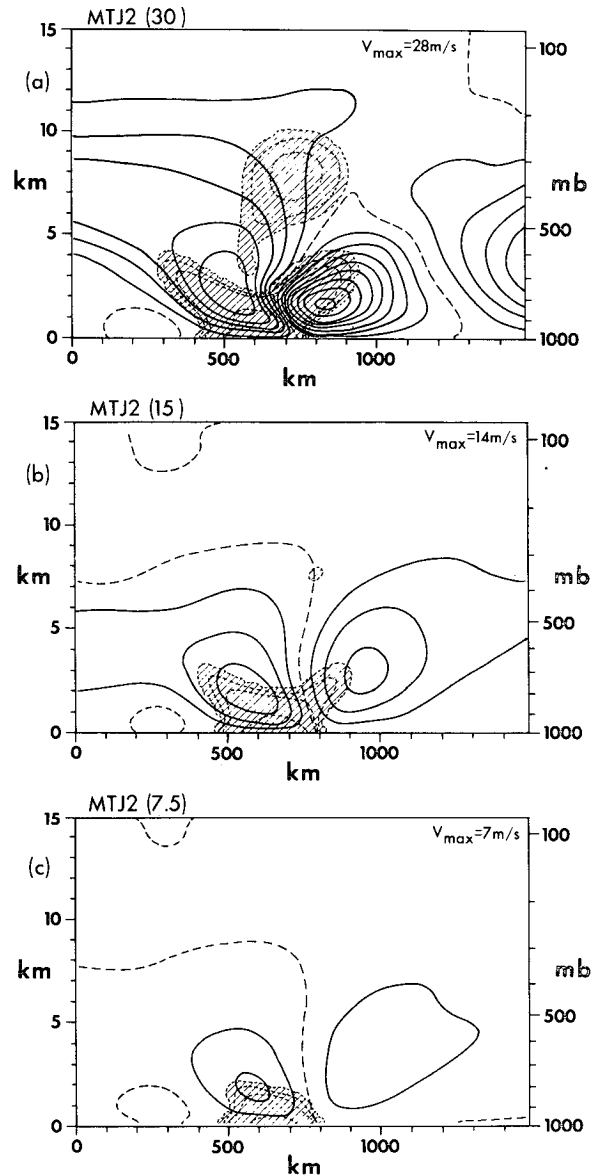Regarding variability of the frontal wind v, Fig. 6

Fig. 6. Comparison of perturbation streamfunction ψ' fields for mid-tropospheric jet cases at time $t = 15.20$ h with different jet intensities V_M. Cross-hatched areas show regions of low $\mathrm{Ri_v}$ as in Fig. 4. The contour interval $\Delta\psi' = 200$ kg (m s)$^{-1}$.

(which is similar to Fig. 4) shows the cross-stream circulation to be proportional to the jet intensity as indicated by the mean area of low $\mathrm{Ri_v}$. Also the direction and the position of the cross-stream vortices are unchanged by changes in $\mathrm{Ri_v}$.

Up to this point, the frontal conditions which have been considered involve a mean cross-stream wind directed to the right with wind intensity increasing with height. An interesting question which naturally arises is: What would be the frontal circulation for the same temperature and y-velocity configuration if the cross-stream wind direction and shear were reversed? Under
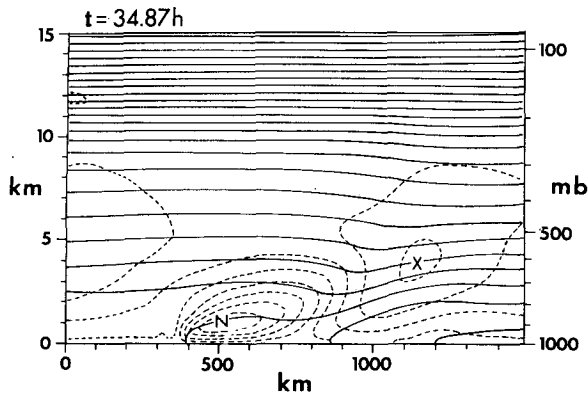
FIG. 7. Contour map of potential temperature θ (solid contours) and perturbation streamfunction ψ' (dashed lines) for warm front case MTJ2W(30) at time $t=34.87$ h. Contour intervals are $\Delta\theta=5°$C and $\Delta\psi'=300$ kg (m s)$^{-1}$. Symbols X and N denote locations of maximum and minimum ψ', respectively.

such a wind reversal, the problem of the cold front evolution considered above is transformed into a study of the evolution of a warm front with the same initial conditions. In fact, the actual case which we will consider here will use the same initial mean wind profile $U_g(z)$ but will use the negative of the initial y-velocity field v of case MTJ2(30) (see Fig. 1b: the field is also transposed in x as Table 1 shows) thereby placing the cold air mass to the right or downwind side of the surface front.

Fig. 7 shows a composite display of contours of perturbation streamfunction (dashed contours) and potential temperature (solid contours) for this warm front mid-tropospheric jet case [which we will designate as MTJ2W(30)] after 34.87 h. The front has been advected to the right and distorted, and as one might expect, the major cross-stream circulation tends to be opposite in direction to that observed in the equivalent cold front [i.e., with $U_g(z)$ reversed]. In particular, whereas the circulation in the cold front case MTJ2(30) tended to produce upward motion within the front, thereby maintaining the front, the circulation in the warm front case MTJ2W(30) produces downward motion in the initial strong baroclinic zone, thus making the evolving front shallower. The horizontal advection of y-momentum in the warm front reduces the vertical shear of v, thereby weakening the horizontal temperature gradient which is in approximate balance with $\partial v/\partial z$.

The front shown in Fig. 7 has decayed so much from its initial state (a mirror image of the initial conditions of Fig. 1b) that one may question whether the initial conditions used were realistic and appropriate for the study of warm front evolution.[1] However, the assumed

---

[1] In fact, the horizontal deformation effect studied by Hoskins and Bretherton (1972) and Williams (1972) is expected to be the predominant mechanism for maintaining the warm front.

initial conditions may be viewed as representing the state of a cold front which has become stationary and then changed to a warm front due to a rapid reversal of the synoptic cross-stream wind direction. Such an argument provides a partial justification for our use of the reversed cold front initial conditions in the warm front solution. On the other hand, given the observed numerical result that the present warm front temperature structure becomes shallower quite rapidly, there is still some question whether the synoptic winds which initially drive the cold front can reverse direction rapidly enough to maintain the cold front structure as must be assumed if the above synoptic wind reversal argument is to apply.

Fig. 7 shows the constant θ lines of the front at 34.87 h to be quite shallow in that portion of the advected warm front which was originally the nose of the front. As stated above, this collapse is due to the strong downward motion which developed in the initial warm front. But this downward flow causes, in turn, a strong divergence at the surface which produces an upwind advection of cold air along the surface. This advection then generates the secondary cold front which is shown in the figure in the convergence zone some 400 km to the left of the primary front.

The strong dependence of the warm front evolution upon initial conditions casts some doubt upon the realism of these results. However, such an evolution could occur under favorable conditions. In fact, it might be speculated that the convergence zone associated with the secondary warm front observed in our solution could reinforce the upward motion in the trailing cold front of an occluding frontal system, thereby enhancing the lifting above such a cold front and increasing the likelihood of deep convection within the occluding frontal system.

4. Discussion of results

In attempting to explain the numerical solutions described in Section 3, one observes from the equation set (2.1)–(2.4a) that the generation of vorticity in the $x-z$ plane depends primarily upon the difference

$$R = f\frac{\partial v}{\partial z} - \frac{g}{\theta_0}\frac{\partial\theta}{\partial x}, \qquad (4.1)$$

where we will refer to R as the "ageostrophic residue" because this difference represents the departure of the y-velocity and potential temperature fields from geostrophic balance. Without losing generality in the present discussion, we will neglect viscous and diffusive terms and will assume that the specific volume α_0 is equal to unity everywhere. Then, differentiation of Eq. (2.3) with respect to x gives

$$\frac{\partial^2\theta}{\partial x\partial t} - J\left(\psi, \frac{\partial\theta}{\partial x}\right) - J\left(\frac{\partial\psi}{\partial x}, \theta\right) + \frac{\partial\theta_g}{\partial y}\frac{\partial v}{\partial x} = 0, \qquad (4.2)$$

while differentiation of Eq. (2.2) with respect to z gives

$$\frac{\partial^2 v}{\partial z \partial t} - J\left(\psi, \frac{\partial v}{\partial z}\right) - J\left(\frac{\partial \psi}{\partial z}, v\right) + f\left(\frac{\partial u}{\partial z} - \frac{\partial U_g}{\partial z}\right) = 0. \quad (4.3)$$

Multiplying Eq. (4.3) by f and Eq. (4.2) by g/θ_0, subtracting, and using the definition (4.1), we obtain an expression for the substantial derivative of the ageostrophic residue R:

$$\frac{DR}{Dt} = -N^2 \frac{\partial^2 \psi}{\partial x^2} - f\left(f + \frac{\partial v}{\partial x}\right)\frac{\partial^2 \psi}{\partial z^2} + \left(2f\frac{\partial v}{\partial z} - R\right)\frac{\partial^2 \psi}{\partial x \partial z}$$

$$+ f\left(f - \frac{\partial v}{\partial x}\right)\frac{\partial U_g}{\partial z}, \quad (4.4)$$

where $N = [(g/\theta_0)\partial\theta/\partial z]^{\frac{1}{2}}$ is the Brunt-Väisälä frequency. The ageostrophic residue R produces vorticity ζ through Eq. (2.1) which may be rewritten, without viscous and diffusive terms, as

$$\frac{D\zeta}{Dt} = R. \quad (4.5)$$

Hence, knowing the behavior of R as described by Eq. (4.4), we can predict the rate of generation of cross-stream vorticity along the front through Eq. (4.5).

a. Front without cross-stream wind

The first frontal case to be considered is that in which there is no initial cross-stream wind, that is, $U_g = 0$. We can investigate the dynamics of this case by linearizing the geostrophic residue equation (4.4) to obtain

$$\frac{\partial R}{\partial t} = -N^2 \frac{\partial^2 \psi}{\partial x^2} - f\left(f + \frac{\partial v}{\partial x}\right)\frac{\partial^2 \psi}{\partial z^2} + 2f\frac{\partial v}{\partial z}\frac{\partial^2 \psi}{\partial x \partial z}, \quad (4.6)$$

where we have neglected the term $R\partial^2\psi/\partial x \partial z$ as second-order. The linearized form of Eq. (4.5) is

$$\frac{\partial \zeta}{\partial t} = R, \quad (4.7)$$

so the combination of (4.6) and (4.7) gives

$$\frac{\partial^2}{\partial t^2}(\nabla^2 \psi) = -N^2 \frac{\partial^2 \psi}{\partial x^2} - f\left(f + \frac{\partial v}{\partial x}\right)\frac{\partial^2 \psi}{\partial z^2} + 2f\frac{\partial v}{\partial z}\frac{\partial^2 \psi}{\partial x \partial z}, \quad (4.8)$$

where we have used the fact that $\zeta = \nabla^2 \psi$. If the horizontal shear $\partial v/\partial x$ of the frontal jet may be neglected as small compared to f, one can show that (4.8) will have unstable solutions if the Richardson number $\mathrm{Ri_v} \equiv N^2/(\partial v/\partial z)^2 < 1$. This instability, known as "symmetric baroclinic instability" or simply "symmetric instability," was first studied by Solberg (1936) and has been investigated further by Stone (1966) and

others. Symmetric instability occurs as particles move in the $x-z$ plane in trajectories which are parallel to the isentropes (lines of constant θ). This particle motion advects y momentum and potential temperature at different rates, thereby producing geostrophic imbalance which generates vorticity. As McIntyre (1970) has shown, geostrophic imbalance also can be produced by differential diffusion of the v and θ fields. Although such phenomena are a form of baroclinic instability, the energy for symmetric instability is taken from the mean kinetic energy of the flow rather than from the potential energy as is the case for the basic baroclinic instability.

In applying these linearized equations to a frontal zone, one finds that the horizontal shear $\partial v/\partial x$ is of the order of the Coriolis parameter f and cannot be neglected. Ooyama (1966) has shown that, in the presence of a weak but finite horizontal shear, the previous condition for instability is modified to the condition

$$\mathrm{Ri_v} < \frac{f}{f + \partial v/\partial x}.$$

Hence the horizontal shear $\partial v/\partial x$'s shown to make the flow more or less stable depending on whether the absolute vertical vorticity $f + \partial v/\partial x$ is larger or smaller than f.

The idealized frontal systems described in Section 3 have zones of $\mathrm{Ri_v} < 1$ within the frontal region which will permit symmetric instability to develop. Such regions correspond to zones of negative total potential vorticity as discussed by Hoskins (1974). These zones could be produced in nature by diabatic or frictional effects which were present during the development of the front. It is not unreasonable to expect that such zones of $\mathrm{Ri_v} < 1$ do exist (although we will show in the discussion which follows that symmetric instability is of little consequence in producing circulations of sufficient intensity to trigger a squall line).

It is important to determine whether symmetric instability does actually occur in the frontal configurations which we have used in the numerical solutions. These conditions in a frontal region are markedly different from the conditions treated in the analysis of Stone since low $\mathrm{Ri_v}$ occurs only in localized regions in the frontal case, whereas $\mathrm{Ri_v}$ is small over the whole field in Stone's case.

As described in Section 3, numerical solutions were obtained for the two frontal configurations when no initial cross-stream wind was present. A small, random streamfunction perturbation [maximum amplitude of 1 kg (m s)$^{-1}$] was applied to the solution initially in order to excite any instabilities within the field.[2] An

---

[2] Because the generation of geostrophic imbalance by diffusion [$(Pr)_e = 0.7$] was much more rapid than that produced by advection from this perturbation, the small streamfunction disturbance was found to have little effect on the circulation which developed.

MIDTROPOSPHERIC JET MTJ1 (30)
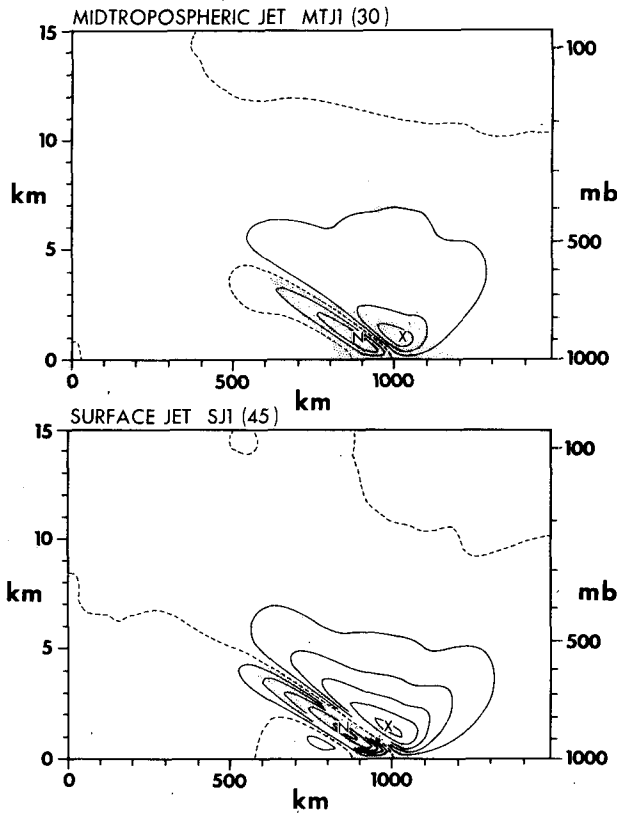

SURFACE JET SJ1 (45)

FIG. 8. Comparison of streamfunction fields at time $t=5.00$ h for cases with no mean cross-stream wind shear. The contour interval $\Delta\psi$ is 30 kg (m s)$^{-1}$. Light and dark stippled areas show regions of $Ri_v<11$ and $Ri_v<1$, respectively. Symbols X and N show locations of maximum and minimum ψ, respectively. For MTJ1(30), the extremes are 107 and -90 kg (m s)$^{-1}$, while for SJ1(45), these are 158 and -159 kg (m s)$^{-1}$.

instability immediately developed in both solutions in the form of two major circulation cells located in the strongly baroclinic zone within the frontal region. Fig. 8 shows the streamfunction contours of the cases SJ1(45) and MTJ1(30) at $t=5$ h, the approximate time of maximum amplitude of the circulation for each case. The cell structure in the most intense baroclinic zone is shown to be oriented so that particle trajectories lie along isentropes, an alignment which is representative of symmetric instability. Also, agreement with the theory of symmetric instability is shown by the occurrence of the most intense circulation in a region of low potential vorticity as denoted in the figure by shaded zones for regions of the low Richardson number (light shading for $Ri_v<11$ and dark shading for $Ri_v<1$). Finally, analysis of the energy budget for the solutions shows the mean kinetic energy of the y-velocity to decrease as the instability develops, a behavior which is typical of symmetric instability.

The full, nonlinear equation system used in the numerical models permits us to study the full evolution of the instability in the frontal zone. Fig. 9 shows the

growth and decay of the cells as presented by the time variation of maximum and minimum values of the streamfunction ψ. The growth rate of the instability is initially very rapid with a doubling time of 0.5 h at time $t=1$ h in each case. However, this growth rate decreases continuously until it vanishes at around 5 h. This decrease in the growth rate appears to be due to the nonlinear advection of the symmetric baroclinic wave out of the zone of low Richardson number in which the symmetric instability initially developed. The advection of air parcels across isentropes near the surface, as shown in Fig. 8, will also tend to alter the symmetric instability growth by drawing energy from potential energy rather than from the mean kinetic energy. The larger maximum amplitude of the circulation in the SJ case compared to the MTJ solution can be explained by the different magnitudes of the horizontal gradient $\partial v/\partial x$ in the low Ri_v regions which will

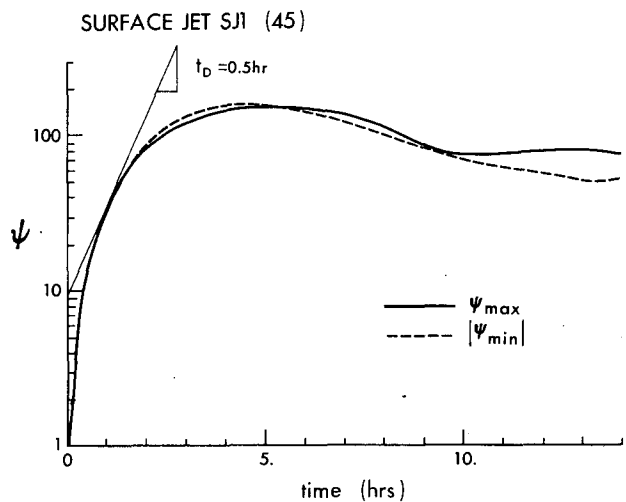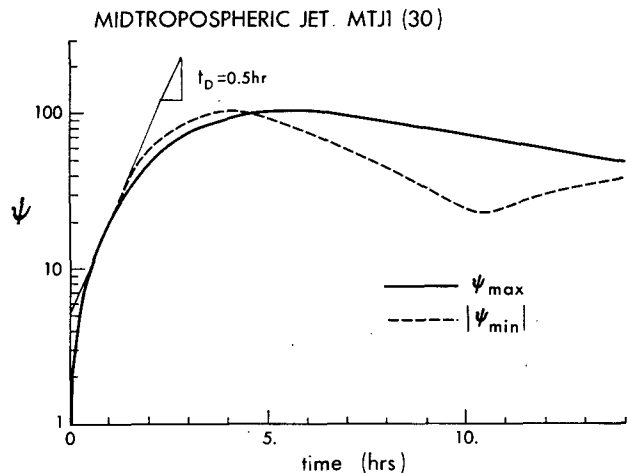MIDTROPOSPHERIC JET. MTJ1 (30)

SURFACE JET SJ1 (45)

FIG. 9. Comparison of time variation of maximum and minimum values of streamfunction for cases MTJ1(30) and SJ1(45) with no mean cross-stream wind. The slope of a line representing a doubling time t_D of 0.5 h is included for reference purposes.

cause the areas in which the quantity Ri_v $(f+\partial v/\partial x)/f$ is small to differ somewhat between the two cases.[3]

The numerical solutions for both frontal cases without cross-stream wind indicate that the circulations produced by the symmetric instability are very weak. Analysis of the velocity fields produced by the cells shown in Fig. 8 indicates horizontal and vertical velocity magnitudes to be less than 0.4 and 0.004 m s^{-1}, respectively. We must therefore conclude that the symmetric instability associated with stationary fronts cannot be an important mechanism for producing cross-stream circulations of an intensity sufficient to trigger a squall line unless the symmetric instability is modified by moisture, surface heating or other parameters not considered here. This result is not surprising since prefrontal squall lines are seldom observed in the vicinity of a stationary front under atmospheric conditions such as those considered in the present paper.

b. Circulation driven by cross-stream wind

The previous numerical results as well as atmospheric observations suggest that the most intense cross-stream circulations occur in fronts which are driven by a large-scale wind blowing across the front. Hence we will look in more detail at these numerical solutions presented in Section 3 in which a cross-stream wind shear is prescribed initially.[4]

The initial tendency of the equation system (2.1)–(2.4) to generate cross-stream circulation can be seen easily by reference to Eqs. (4.4) and (4.5) including the initial shear $\partial U_g/\partial z$. Since the numerical solution begins at $t=0$ with geostrophic balance, the ageostrophic residue R will initially be zero. Then the substantial derivative of R at $t=0$ will be simply

$$\frac{DR}{Dt} = -2f\frac{\partial v}{\partial x}\frac{\partial U_g}{\partial z} \qquad (4.9)$$

since the streamfunction ψ at this time only involves the geostrophic wind U_g. This equation shows that the initial geostrophic departure R will depend on the magnitude and sign of $\partial v/\partial x$. Without loss of generality, we will assume $\partial U_g/\partial z$ to be positive everywhere (as is

---

[4] It should be recognized that a stationary front whose axis is not normal to the x-z plane of the numerical model will have a cross-stream geostrophic wind U_g as well as a geostrophic y-velocity V_g in the reference frame of the model but, of course, will not produce an advection of the front in the x-direction. In order for this to occur, the wind fields U_g and V_g must have a very special relationship, namely, that U_g be proportional to V_g. Such cases are excluded in the discussion which follows.

[3] It is important to recognize the fact that the presence of low $f+\partial v/\partial x$ in a region does not guarantee that symmetric instability will occur there. What is important is that the local intensity of the geostrophic balance be large, as indicated by a large vertical shear $\partial v/\partial z$ and therefore by a small Richardson number Ri_v with $f+\partial v/\partial x$ only acting to modify the instability

the case in the solutions considered here). Then an area of negative $\partial v/\partial x$ will produce a positive R and a positive vorticity (local minimum in ψ') as shown by Eq. (4.5), while an area of positive $\partial v/\partial x$ will produce negative R and negative ζ (local maximum in ψ'). This result is verified in Figs. 2 and 5 in which the early fields show regions of negative and positive $\partial v/\partial x$ corresponding to regions of negative and positive ψ', respectively, for both the SJ and the MTJ cases. Although this explanation of the solution trends cannot extend beyond initial times, the numerical solutions show that cells generated in this way persist to later times, ultimately reaching a quasi-equilibrium state between the ageostrophic state in the frontal zone and the upstream condition for the mean shear flow. Indeed, it appears that the initial conditions of the numerical solution are not crucial to the major part of the circulation within the frontal system, but rather the cross-stream wind and the frontal jet configuration will determine the cross-stream circulation except for weaker inertial gravity wave oscillations which are superimposed on this circulation and which may depend upon the initial conditions.

In fact, assuming an equilibrium situation in which the cross-stream circulation is balanced by the ageostrophic departure of the frontal zone, Eq. (4.4) will describe this equilibrium state if DR/Dt is set to zero so long as the synoptic driving term $\partial U_g/\partial z$ is included. One can further assume that the ageostrophic residue R is very small compared to the term $f(\partial v/\partial z)$. Note, however, that this does not imply that R is unimportant. To see the importance of R to the cross-stream circulation, one may write the expression for potential vorticity q in the present frontal case as

$$q=\left(f+\frac{\partial v}{\partial x}\right)\frac{1}{\theta_0}\frac{\partial\theta}{\partial z}-\frac{1}{\theta_0}\frac{\partial v}{\partial z}\frac{\partial\theta}{\partial x}+\frac{1}{\theta_0}\frac{\partial u}{\partial z}\frac{\partial\theta_g}{\partial z}$$

or, using Eq. (4.1) and the thermal wind expression $\partial U_g/\partial z$,

$$q=\frac{1}{g}\left[\left(f+\frac{\partial v}{\partial x}\right)N^2-f\left(\frac{\partial v}{\partial z}\right)^2-f\left(\frac{\partial U_g}{\partial z}\right)^2\right.$$
$$\left.+\frac{\partial v}{\partial z}R-f\frac{\partial U_g}{\partial z}\zeta'\right]. \qquad (4.10)$$

Inspection of the numerical solutions at successive times shows that conservation of potential vorticity q within advecting air parcels is achieved with a major balance between the first three terms on the right-hand side; however, the smaller ageostrophic residue term $(\partial v/\partial z)R$ is found to be of the same order as the last term involving the cross-stream ageostrophic vorticity ζ'. The balance of the smaller quantity R with ζ' in this equation is possible because R is multiplied by $\partial v/\partial z$, while ζ' is multiplied by $\partial U_g/\partial z$, where $\partial v/\partial z$ is much

MODEL SOLUTION

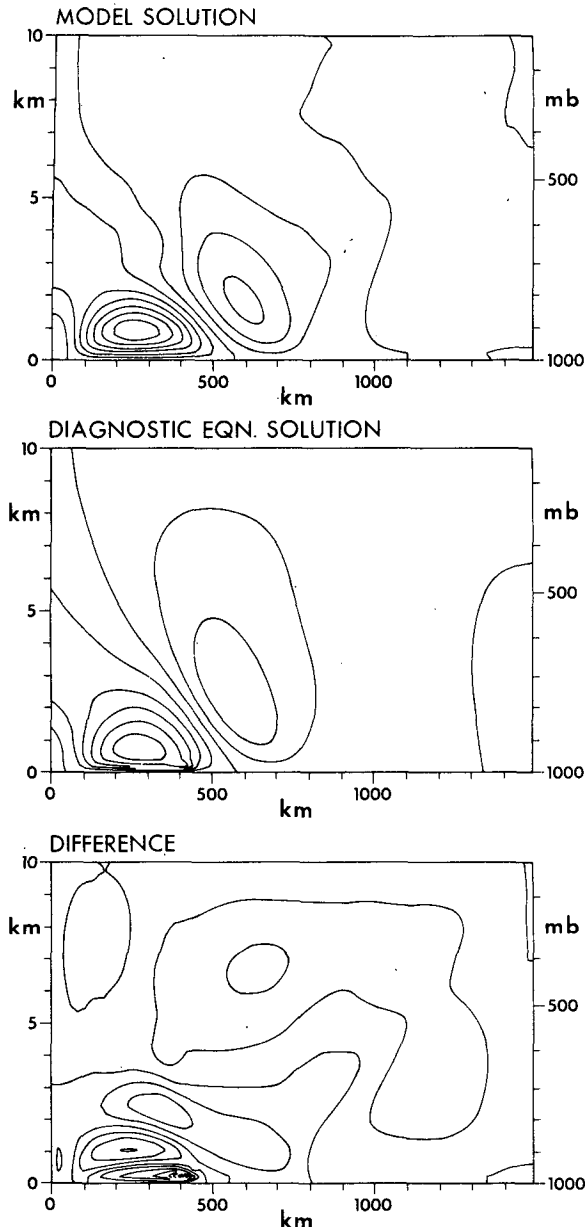DIAGNOSTIC EQN. SOLUTION

DIFFERENCE

FIG. 10. Comparison of perturbation streamfunction fields at time $t = 16.77$ h for surface jet case equivalent to SJ3(45) but with constant vertical grid spacing. Top frame shows result of model solution, while center frame is solution obtained from the diagnostic equation (4.11). Lower frame shows difference between model and diagnostic equation solutions for ψ'. Contour interval for top and middle frames is $\Delta\psi' = 304$ kg (m s)$^{-1}$ while value for lower frame is $\Delta\psi' = 132$ kg (m s)$^{-1}$.

larger than $\partial U_g/\partial z$. In fact, this approximate balance of the last two terms in (4.10) implies that one can obtain a reasonable estimate of the ageostrophic residue R by knowing the cross-stream circulation within the frontal zone.

Returning to Eq. (4.4), if one assumed that DR/Dt and R can be neglected, then a diagnostic equation is

obtained for the cross-stream circulation as a function of the y-velocity field within the frontal zone and the driving wind shear $\partial U_g/\partial z$:

$$N^2 \frac{\partial^2 \psi}{\partial x^2} + f\left(f + \frac{\partial v}{\partial x}\right)\frac{\partial^2 \psi}{\partial z^2} - 2f\frac{\partial v}{\partial z}\frac{\partial^2 \psi}{\partial x \partial z}$$

$$= f\left(f - \frac{\partial v}{\partial x}\right)\frac{\partial U_g}{\partial z}. \quad (4.11)$$

This equation is similar to the quasigeostrophic equation originally studied by Sawyer (1956) and Eliassen (1962).

A solution of the diagnostic equation for the surface jet case at time $t = 16.8$ h is shown in Fig. 10 in comparison with the perturbation streamfunction obtained from the numerical solution at this time. Comparison of the model solution and the diagnostic equation solution in the top two frames of this figure indicates the similarity between the two results. The locations of the two primary circulation cells within the frontal zone are predicted well by the diagnostic equation with the magnitudes of the streamfunction in the diagnostic solution differing from the magnitudes in the model solution by less than 15%. The difference between the diagnostic solution and the full numerical solution is shown in the bottom frame. This difference is primarily an inertial-gravity wave type oscillation and will depend upon the initial imbalance in the fields in the early stages of the solution. The good agreement of the diagnostic solution with the model solution shows that Eq. (4.11) will indicate the dependence of the cross-stream circulation upon parameters such as the vertical wind shear $\partial U_g/\partial z$, the horizontal shear $\partial v/\partial x$ and the Richardson number Ri$_v$, as was investigated in Section 3.

5. Conclusion

After investigating the cross-stream circulation in two different frontal configurations and for different shears in the cross-stream flow, we conclude that symmetric instability waves can be excited in regions of Richardson number Ri$_v < 1$. However, the resulting circulation is quite weak unless Ri$_v$ becomes unrealistically low.

On the other hand, in a moving frontal system, the synoptic wind with shear will advect the potential temperature and y-velocity fields differently in the vertical. As a consequence of this sheared advection, the vertical shear $\partial v/\partial z$ and the horizontal gradient $\partial\theta/\partial x$ will be advected at different rates, thereby producing an ageostrophic residue in the thermal wind relation which generates a cross-stream circulation. In all of the cold front cases studied, this circulation was found to maintain the surface discontinuity, while in the single warm front case considered, the resulting

circulation caused the surface front to weaken. The intensity of the cross-stream circulation of a moving front under certain synoptic conditions can be strong enough to produce lifting which triggers a squall line in a moist unstable atmosphere. The generation of a squall line under such conditions will be discussed by Ross and Orlanski (1977).

The circulation which is produced by the cross-stream wind shear ultimately reaches a quasi-steady state, which is independent of the initial conditions of the numerical solution and depends only on the frontal configuration and the intensity of the shear in the synoptic wind directed across the front. The diagnostic equation (4.11) gives a good estimation of this cross-stream circulation. Superimposed on this circulation is a weaker oscillating circulation associated with inertial-gravity waves which were generated primarily by the initial adjustment of the numerical solution. It should be pointed out that actual cold fronts may exhibit waves of similar scales which were created during the active period of frontogenesis or were initiated by diabatic heating, friction, orographic effects or other non-geostrophic perturbations which the frontal system might encounter. Such transitory disturbances may enhance or retard moist convection. However, we believe that the quasi-steady circulation produced by cross-stream wind shear can have sufficient intensity by itself to trigger squall line formation under favorable moisture conditions.

REFERENCES

Arakawa, A., 1966: Computational design for long-term numerical integration of the equations of motion: Two dimensional incompressible flow, Part I. *J. Comput. Phys.*, **1**, 119–143.

Bjerknes, J., 1919: On the structure of moving cyclones. *Geofys. Publik.*, **1**, 1–8.

——, and C. Godske, 1936: On the theory of cyclone formation at extra-tropical fronts. *Astrophys. Norv.*, **1**, 199–235.

Eliassen, A., 1962: On the vertical circulation in frontal zones. *Geofys. Publik.*, **24**, 147–160.

Hoskins, B. J., 1974: The role of potential vorticity in symmetric stability and instability. *Quart. J. Roy. Meteor. Soc.*, **100**, 480–482.

——, and F. P. Bretherton, 1972: Atmospheric frontogenesis models: Mathematical formulation and solution. *J. Atmos. Sci.*, **29**, 11–37.

Lilly, D. K., 1965: On the computational stability of numerical solutions of time dependent non-linear geophysical fluid dynamics problems. *Mon. Wea. Rev.*, **93**, 11–26.

McIntyre, M. E., 1970: Diffusive destabilization of the baroclinic circular vortex. *Geophys. Fluid Dyn.*, **1**, 19–57.

Ogura, Y., and N. A. Phillips, 1962: Scale analysis of deep and shallow convection in the atmosphere. *J. Atmos. Sci.*, **19**, 173–179.

Ooyama, K., 1966: On the stability of the baroclinic circular vortex: A sufficient criterion for instability. *J. Atmos. Sci.*, **23**, 43–53.

Orlanski, I., 1976: A simple boundary condition for unbounded hyperbolic flows. *J. Comput. Phys.*, **21**, 251–269.

——, and B. B. Ross, 1973: Numerical simulation of the generation and breaking of internal gravity waves. *J. Geophys. Res.*, **78**, 8808–8826.

——, B. B. Ross and L. J. Polinsky, 1974: Diurnal variation of the planetary boundary layer in a mesoscale model. *J. Atmos. Sci.*, **31**, 965–989.

Richtmyer, R. D., and K. W. Morton, 1967: *Difference Methods for Initial-Value Problems*, 2nd ed. Interscience, 405 pp.

Ross, B. B., and I. Orlanski, 1977: The circulation associated with a cold front. Part II: Moist case. *J. Atmos. Sci.* (in press).

Sanders, F., 1955: An investigation of the structure and dynamics of an intense surface frontal zone. *J. Meteor.*, **12**, 542–552.

Sawyer, J. S., 1956: The vertical circulation at meteorological fronts and its relation to frontogenesis. *Proc. Roy. Soc. London*, **A234**, 346–362.

Solberg, H., 1936: Le mouvement d'inertie de l'atmosphere stable et son role dans la theorie des cyclones. *Proc.-verb. Assoc. Meteor.* U.G.G.I. (Edinburgh), Part II (Memoires), 66–82.

Stone, P., 1966: On non-geostrophic baroclinic instability. *J. Atmos. Sci.*, **23**, 390–400.

Williams, R. T., 1967: Atmospheric frontogenesis: A numerical experiment. *J. Atmos. Sci.*, **24**, 627–641.

——, 1972: Quasi-geostrophic versus non-geostrophic frontogenesis. *J. Atmos. Sci.*, **29**, 3–10.

——, 1974: Numerical simulation of steady-state fronts. *J. Atmos. Sci.*, **31**, 1286–1296.

Young, D., 1971: *Iterative Solution of Large Linear Systems.* Academic Press, 570 pp.